applied optics

Diel changes of the optical backscattering coefficient of oceanic particulate matter determined from diel changes in apparent optical properties: a case study in the Mediterranean Sea (BOUSSOLE site)

Malika Kheireddine,[1,*] David Antoine,[2,3] Vincenzo Vellucci,[4] and Bernard Gentili[3]

[1]King Abdullah University of Science and Technology, Red Sea Research Center (RSRC), Biological and Environmental Sciences and Engineering Division (BESE), Thuwal, 23955-6900, Saudi Arabia
[2]Remote Sensing and Satellite Research Group, School of Earth and Planetary Sciences, Curtin University, Perth, WA 6845, Australia
[3]Sorbonne Université, CNRS, Laboratoire d'Océanographie de Villefranche, LOV, F-06230, Villefranche-sur-Mer, France
[4]Sorbonne Université, CNRS, Institut de la Mer de Villefranche, IMEV, F-06230, Villefranche-sur-Mer, France
*Corresponding author: malika.kheireddine@kaust.edu.sa

Received 15 February 2022; revised 26 May 2022; accepted 29 May 2022; posted 31 May 2022; published 27 June 2022

Using *in situ* measurements of radiometric quantities and of the optical backscattering coefficient of particulate matter (b_{bp}) at an oceanic site, we show that diel cycles of b_{bp} are large enough to generate measurable diel variability of the ocean reflectance. This means that biogeochemical quantities such as net phytoplankton primary production, which are derivable from the diel b_{bp} signal, can be potentially derived also from the diel variability of ocean color radiometry (OCR). This is a promising avenue for basin-scale quantification of such quantities because OCR is now performed from geostationary platforms that enable quantification of diel changes in the ocean reflectance over large ocean expanses. To assess the feasibility of this inversion, we applied three numerical inversion algorithms to derive b_{bp} from measured reflectance data. The uncertainty in deriving b_{bp} transfers to the retrieval of its diel cycle, making the performance of the inversion better in the green part of the spectrum (555 nm), with correlation coefficients >0.75 and a variability of 40% between the observed and derived b_{bp} diel changes. While the results are encouraging, they also emphasize the inherent limitation of current inversion algorithms in deriving diel changes of b_{bp}, which essentially stems from the empirical parameterizations that such algorithms include.

https://doi.org/10.1364/AO.456216

1. INTRODUCTION

Recording from space the changes of the ocean reflectance from dawn to dusk becomes a realistic target with the advent of ocean color sensors on geostationary satellites. The Korean Geostationary Ocean Color Imager (GOCI, [1]) has opened the way since 2010, followed by its successor GOCI-II in 2020 [2,3], and other instruments are announced for launches in the 2020 decade (e.g., the NASA Geosynchronous Littoral Imaging and Monitoring Radiometer [4]). Such missions can typically record the ocean reflectance hourly throughout the course of a day, either targeting specific areas or embracing the full Earth disk [5]. Taking full advantage of these high-frequency top-of-atmosphere observations requires numerical inversion techniques capable of retrieving geophysical properties of interest with a consistently high accuracy under the changing observation conditions encountered during a day [6].

This work addresses the question as to whether the changes of ocean inherent optical properties (IOPs) that occur during the course of a day are derivable from the changes in reflectance as potentially recorded from a geostationary satellite sensor. This quest stems from evidence of such changes in IOPs observed *in situ*, in particular for the particulate optical backscattering coefficient, b_{bp} [7–10]. These diel changes of b_{bp} can be used as a proxy of the accumulation or loss of particulate organic carbon in the euphotic zone through the photosynthesis–respiration balance [8,11], and then as a proxy of net community production [7,12–16]. Therefore, if the b_{bp} diel variability can be quantified from space from the diel changes in reflectance, a new

way is opened for determination of net community production at large scale from satellite observations.

In open ocean Case I waters (as per [17]), b_{bp} typically increases from sunrise to about 2–4 h before sunset, and then decreases until next sunrise [18]. The amplitude of this cycle is determined by changes in concentrations, size structure, and refractive index of the different populations of particles, and of phytoplankton in particular. Although the term *diel changes* normally refers to changes involving a 24-hour period that includes a day and the adjoining night, it will be used hereafter for the sake of conciseness to refer to the changes of b_{bp} that occur during daylight only.

The questions to be addressed are (1) whether the b_{bp} diel cycle observed *in situ* generates a measurable diel variability in reflectance and, assuming the answer is positive, (2) whether the diel b_{bp} cycle can be retrieved from existing numerical inversion algorithms of the reflectance spectrum also measured *in situ* at different times of the day and, (3) whether (2) is still feasible when the reflectance is derived from satellite ocean color radiometry. This paper only addresses points (1) and (2).

It is stressed here that correctly retrieving the amplitude of the diel cycle is somehow little dependent on the absolute accuracy of b_{bp} retrievals, provided that the associated uncertainties do not change significantly for retrievals carried out from reflectances measured at different times of a day (so for various Sun elevations).

These questions were addressed by using high-frequency (every 15 min) field observations of b_{bp}; the irradiance reflectance, R; the diffuse attenuation coefficient for downward irradiance, K_d; and the remote-sensing reflectance, R_{rs}, performed at the BOUée pour l'acquiSition d'une Série Optique à Long termE site in the Mediterranean Sea (BOUSSOLE [19,20]). Contrary to what was done by Kheireddine and Antoine [18] using the same dataset, average seasonal patterns are not aimed at here. A few case studies have been selected to answer question (1) above, and to illustrate the first challenge in answering question (2).

It must be kept in mind that no fully analytical bio-optical model exists that would allow making fully explicit the dependence of reflectance on IOPs plus the environment conditions (the Sun zenith angle in particular). Therefore, our goal here is precisely to assess whether existing semi-analytical algorithms still can be used for deriving diel variability of b_{bp} from diel variability of reflectance. We do not claim that we have selected the most appropriate models to perform these retrievals. Instead, we have selected among the most popular methods in order to study their relevance to this specific objective.

2. DATA AND METHODS

A. Field Measurements and Sampling

1. Description of the BOUSSOLE Site and Related Field Operations

Essential information about the site characteristics, the measurement platforms and the instrumentation is provided in [19–21]. Only few elements relevant to the present work are reminded. The BOUSSOLE site is located in deep waters (2440 m) of the Ligurian Sea, one of the sub-basins of the northwestern Mediterranean Sea. An important seasonality exists in physical conditions, with deep mixed layers in winter (∼400 m, sometimes down to the bottom), and a marked stratification during summer. This seasonal dynamics drives the seasonal changes in trophic levels from oligotrophy in summer to bloom conditions in spring. There is, accordingly, a large range of optical properties at this site. A buoy has been permanently deployed at the BOUSSOLE site since September 2003 and operates in a quasi-continuous mode, with data acquisition sequences of one minute every 15 min night and day. This platform was specifically designed to measure radiometric quantities in the water column (nominally at 4 m and 9 m), and above the surface (4.5 m above sea level), from which apparent optical properties (AOPs) are derived, typically the irradiance reflectance, R, the remote-sensing reflectance, R_{rs}, and the diffuse attenuation coefficient for downward irradiance, K_d. IOPs, including b_{bp}, are collected at the same depths in the water column. Two sister buoys equipped with the same set of instruments are used, with rotation performed about every 6 months. The site is visited monthly for buoy servicing, during which 0–400 m CTD casts are performed for acquisition of hydrological data (conductivity, temperature, and pressure), IOPs, and water sampling for subsequent phytoplankton pigment analyses and particulate absorption measurements [22].

2. Particulate Backscattering Coefficient

The total angular scattering coefficient at 140°, $\beta(\lambda)(140)$, was measured at BOUSSOLE using a Hydro-Optics, Biology, and Instrumentation Laboratories (HOBI Labs) Hydroscat-4 backscattering meter installed at 9 m and equipped with filters at 443, 488, 555, and 620 nm. The instrument faceplate is made of copper, which has proven to fully prevent biofouling. The instrument operates at 1 Hz, so that about 60 measurements are collected during each of the 1 min data collection sequences.

The median of these 60 measurements is used to derive a representative value for $\beta(\lambda)(140)$. Dark current measurements are performed on site by divers with a black neoprene cap covering the instrument windows. Their average for a given 6 month deployment are subtracted from the raw $\beta(\lambda)(140)$ measurements. The $\beta(\lambda)(140)$ values are also corrected for attenuation along the measurement path (the $\sigma(\lambda)$ correction of Maffione and Dana [23]) using the beam attenuation coefficient measured in parallel (see below) and the total absorption coefficient derived from inversion of K_d and R (Eqs. 12 and 13 in [24]). The $b_{bp}(\lambda)$ coefficient is derived from the corrected $\beta(\lambda)(140)$ as follows [25]:

$$b_{bp}(\lambda) = 2\pi\,\chi_p\,(\beta(\lambda)(140) - \beta_w(\lambda)(140))\,\left(\mathrm{m}^{-1}\right), \quad \textbf{(1)}$$

where $\chi_p = 1.13$ [26] and where $\beta_w(\lambda)(140)$, the contribution of pure seawater scattering at 140°, is computed following [27,28] using the temperature and salinity measured at the same depth with a Seabird SBE-37SI CTD sensor. All results shown in this paper use the b_{bp} values at 555 nm and 443 nm.

The particulate organic carbon, POC, is derived from b_{bp} at 555 nm following Loisel *et al.* [10]:

$$\mathrm{POC} = 37750\,b_{bp}(555) + 1.3(\mathrm{mg\,m^{-3}}). \quad \textbf{(2)}$$

3. Particulate Beam Attenuation Coefficient

The transmittance (Tr, %) at 650 nm is measured at BOUSSOLE at 4 and 9 m with 25 cm-pathlength Western Environmental Technology Laboratories (Wet Labs) C-Star transmissometers (acceptance angle is 1.2°). Instruments are factory calibrated with de-ionized, ultra-filtered, UV screened water. The transmissometers operate at 6 Hz so that about 360 measurements are collected during each of the 1 min data collection sequence. The median of these 360 measurements is kept as representative of the 1 min record. Note that only the data collected at 9 m depth have been used in this study. The corresponding particulate beam attenuation coefficient, c_p, is then calculated as

$$c_p(650) = -\frac{1}{0.25}\ln\left(\frac{\mathrm{Tr}}{100}\right)\left(\mathrm{m}^{-1}\right). \tag{3}$$

This method assumes that non-water absorption, by colored dissolved organic matter in particular, is negligible at 650 nm [29]. The instrument bodies are covered with copper tape. Source and detector windows are equipped with copper rings and are cleaned about every 2 weeks by divers using soft brushes. These measures have proven efficient in preventing biofouling in most cases. Possible remaining corrupted data are identified from the comparison of data collected before and after cleaning operations. They are eliminated and not used here.

The same instruments are deployed on the monthly casts, and their measurements are used to correct for possible calibration bias or drifts in the buoy transmissometer data.

4. Particulate Backscattering Ratio

The backscattering ratio, $\tilde{b}_{bp}(\lambda)$, is derived from $b_{bp}(\lambda)$ and $c_p(650)$ as follows:

$$\tilde{b}_{bp}(\lambda) = \frac{b_{bp}(\lambda)}{c_p(650)\left(\frac{\lambda}{650}\right)^n}\ \text{(adimensional)}, \tag{4}$$

which assumes that $c_p(650)$ is equal to the particle scattering coefficient at 650 nm, $b_p(650)$ (negligible absorption). This assumption was validated by particulate absorption measurements using the quantitative filter pad technique, which show an average $a_p(650)$ contribution to $c_p(650)$ of 2.5% only. The spectral dependence (exponent n) is derived from chlorophyll a as per [30], with changes from -1 to 0 when [Chl] increases from 0.02 to 2 mg m^{-3}. These values are consistent with measurements made with a Wet Labs AC-9 during the BOUSSOLE cruises (Antoine *et al.* [19]). Errors on the exponent within the $[-1, 0]$ range would entail uncertainties of about 10% on deriving $b_{bp}(\lambda)$ over the spectral distance here considered.

5. Phytoplankton Pigments

Discrete sampling is performed during the BOUSSOLE cruises between the surface and 200 m. Seawater samples are collected from Niskin bottles and filtered through 25 mm diameter Whatman GF/F filters (0.7 µm retention capacity), stored in liquid nitrogen during the cruise, and then transferred at −80°C in the laboratory until algae pigment contents are measured using high-performance liquid chromatography, following [31]. The total chlorophyll a concentration ([Chl]) is computed as the sum of the concentrations of Chl a, chlorophyllide a, and divinyl Chl a. The data obtained from samples at 5 m and 10 m are used here.

6. Radiometric Quantities and Apparent Optical Properties

All radiometric measurements described hereafter were collected using Satlantic OCI-200 Series radiometers. They are placed at the extremity of horizontal arms on the buoy for measuring the downward and the upward irradiance, E_d and E_u, and the upwelling nadir radiance, L_u, at 4 and 9 m, and also on the top of the buoy (4.5 m a.s.l.) to measure the above-surface downward irradiance, E_s. These radiometers are equipped with seven cosine collectors at different spectral bands (412, 443, 490, 510, 555, 665, and 680 nm). The underwater instruments containers are covered with copper tape to protect them against biofouling, and divers clean the optical surfaces about every 2 weeks. These radiometers operate at 6 Hz so that about 360 measurements are collected during each of the 1 min data collection sequences. The median value of each 1 min record is kept as representative of the measurement. An average dark current value is computed from data collected during nighttime and is subtracted from all measurements.

From these measurements, the irradiance reflectance is determined as (wavelength dependence omitted in what follows)

$$R = \frac{E_u(0^-)}{E_d(0^-)}\ \text{(adimensional)}, \tag{5}$$

where $E_d(0^-)$ is the downward irradiance just below the sea surface. It is calculated as E_s reduced by transmission across the air–water interface, i.e., E_s times 0.97 [32]. The upward irradiance just beneath the surface, $E_u(0^-)$, is obtained from

$$E_u(0^-) = E_u(z_4)e^{K_u Z_4}\left(\mu\mathrm{W\,cm^{-2}\,nm^{-1}}\right), \tag{6}$$

where z_4 is the depth of the shallowest buoy arm (nominally at 4 m) and K_u is the diffuse attenuation coefficient for the upward irradiance. K_u is computed from the measurements of E_u collected at the two buoy measurement depths:

$$K_u = -\frac{1}{\Delta z}\,ln\left(\frac{E_u(z_9)}{E_u(z_4)}\right)\ (\mathrm{m}^{-1}), \tag{7}$$

where z_9 is the depth of the deepest buoy arm (nominally at 9 m) and $\Delta z = z_9 - z_4$.

The remote-sensing reflectance, R_{rs}, is computed as

$$R_{rs} = \frac{L_w}{E_s}\ (\mathrm{sr}^{-1}), \tag{8}$$

where E_s is the above-surface downward solar irradiance and the water-leaving radiance, L_w, is computed as

$$L_w = L_u(0^-)\,\frac{1-\rho}{n^2}\ \left(\mu\mathrm{W\,cm^{-2}\,nm^{-1}\,sr^{-1}}\right), \tag{9}$$

where ρ is the water–air reflection coefficient (set to 0.043), and n is the refractive index of seawater (1.34).

$L_u(0^-)$ is obtained as

$$L_u\left(0^-\right) = L_u(Z_4)\,e^{K_{Lu}Z_4}\ \left(\mu\mathrm{W\,cm^{-2}\,nm^{-1}}\right), \tag{10}$$

where

$$K_{Lu} = -\frac{1}{\Delta z} \ln\left(\frac{L_u(z_9)}{L_u(z_4)}\right) \ (\mathrm{m}^{-1}). \quad (11)$$

The diffuse attenuation coefficient for the downward irradiance in the upper layers is computed as

$$K_d = -\frac{1}{Z_9} \ln\left(\frac{E_d(Z_9)}{E_d(0^-)}\right) \ (\mathrm{m}^{-1}). \quad (12)$$

The effect of buoy and instrument self-shading on underwater radiometers was determined with the *SimulO* 3D backward Monte Carlo code [33] and corrected through lookup tables generated for individual instrument geometries [34], whereas extrapolation errors on $L_u(0^-)$ and $E_u(0^-)$ are corrected trough lookup tables [20] generated with *HydroLight* code [35].

Because K_d significantly depends on the Sun zenith angle, θ_s, its normalized values are also computed as follows:

$$K_{d,n} = K_d * \mu_d(\theta_s, [\mathrm{Chl}]) \ (\mathrm{m}^{-1}), \quad (13)$$

where μ_d is the average cosine of the downward irradiance and is taken from precomputed lookup tables generated through *HydroLight* radiative transfer computations including Raman emission and a [Chl]-varying volume scattering function (VSF) for particles [36]. The full dependence of K_d on the Sun zenith angle and IOPs is therefore taken into account.

There is no need for such a correction for R_{rs}, which by definition [Eq. (8)] already includes this normalization.

The photosynthetically available radiation (PAR) was also measured above the surface (4.5 m a.s.l.) by a Satlantic PAR sensor (400–700 nm, μmol quanta $\mathrm{m}^{-2}\ \mathrm{s}^{-1}$).

B. Inversion Algorithms

Three algorithms have been used to derive IOPs from numerical inversion of AOPs, in an attempt to evaluate the uncertainties related to algorithm formulation. The first one was developed by Morel *et al.* [24] (MOR in the following) and allows deriving total absorption, a, and total backscattering, b_b, from R and K_d. This approach combines two equations [37–39] (wavelength omitted):

$$K_d = 1.0395 \frac{a + b_b}{\mu_d(\theta_S, \ [\mathrm{Chl}])} \ (\mathrm{m}^{-1}), \quad (14)$$

and

$$R = f'(\theta_S, \ [\mathrm{Chl}]) \frac{b_b}{a + b_b}, \quad (15)$$

where μ_d is as described above [Eq. (13)] and f' is a factor that conceals dependencies of R on the Sun zenith angle and the IOPs [40]. A precomputed lookup table is derived from the same radiative transfer simulations as for K_d.

Combining Eqs. (14) and (15) leads to

$$b_b = 0.962\, \mu_d(\theta_s, [\mathrm{Chl}])\, K_d (R / f'(\theta_s, [\mathrm{Chl}])) \ (\mathrm{m}^{-1}), \quad (16)$$

and

$$a = 0.962\, \mu_d(\theta_s, [\mathrm{Chl}])\, K_d \left(1 - R / f'(\theta_s, [\mathrm{Chl}])\right) \ (\mathrm{m}^{-1}). \quad (17)$$

The second inversion algorithm that was used is version 6 of the quasi-analytical algorithm (QAA, [41]), which uses R_{rs} as input quantity. Briefly, the total absorption spectrum is first derived from R_{rs}, after selecting a reference wavelength (555 or 667 nm). The calculation of absorption and backscattering are propagated to other wavelengths, assuming that the particulate backscattering varies spectrally in a power-law function [42]. The non-water absorption and backscattering coefficients are derived without any assumption about the spectral shapes of the absorption coefficients of each constituent.

The third algorithm is the GSM semi-analytical bio-optical model [43,44], which also uses R_{rs} as input quantity. GSM is based on the quadratic relationship between R_{rs} and the absorption and backscattering coefficients from [42], which assumes known spectral shapes for specific absorption coefficients of phytoplankton, dissolved and detrital matters, and specific backscattering coefficients for particles. GSM simultaneously retrieves [Chl], the combined absorption coefficient of the particulate and dissolved organic material at 443 nm, and the b_{bp} at 443 nm (b_{bp} at other wavelengths is derived from a power law of wavelength with exponent 1.0337 [45]).

The Lee *et al.* [46] empirical Raman scattering correction was applied to R_{rs} measurements before they are given as inputs to the QAA and GSM algorithms. Such a correction is not needed for MOR because the f' and μ_d lookup tables were generated from radiative transfer simulations including Raman scattering.

Whatever the algorithm, the particulate backscattering coefficient is obtained by removing the water contribution from the total b_b, in the same way than for the *in situ* measurements (i.e., from [27,28]).

C. Radiative Transfer Computations

The consistency between diel changes of the measured AOPs and measured b_{bp} was verified through radiative transfer computations, before AOPs are introduced into inversion algorithms.

In this optical closure exercise, radiative transfer simulations are parameterized with IOPs that follow the observed diel patterns as measured *in situ* at BOUSSOLE for two wavelengths (443 and 555 nm). The values of R, K_d, and R_{rs} obtained from these simulations can then be compared with the observations.

The *HydroLight* code [37] has been used, which solves the radiative transfer equation through the invariant imbedding technique and includes Raman scattering. Input parameters to *HydroLight* were set as follows.

(1) Absorption and scattering coefficients of pure seawater, as well as the molecular phase function are known and prescribed in the code [47,48]. They are kept constant throughout the day.
(2) The non-water absorption coefficient of the water body is unknown (not measured). Therefore, it was computed following [30], which uses the irradiance and the diffuse attenuation for downward irradiance to determine the total non-water absorption from [Chl] (Eqs. (8) to (14) in [30]). It was kept constant whatever the time of the day given that only one [Chl] value per day was available, implicitly assuming no diel changes in the non-water absorption. The high-frequency chlorophyll *a* fluorescence measurements

collected at BOUSSOLE cannot be used to infer possible daily changes in [Chl] because of non-photochemical quenching of fluorescence.

(3) For particulate scattering, the measured particle attenuation coefficient at 650 nm, $c_p(650)$, is used as a proxy for $b_p(650)$. A spectral dependence is applied to get b_p at 443 and 555 nm, following Eq. 14 in [30], where the spectral dependence is expressed as a power law whose exponent varies from −1 to 0 when [Chl] increases from ∼0.02 to ∼2 mg m^{-3}.

(4) The scattering phase function of the particulate matter was derived from the [Chl]-dependent parameterization in [36]. This parameterization was run for each time step using the [Chl] value that led to a VSF with the same $\tilde{b}_{bp}(\lambda)$ as the measured value. By doing so, the diel cycle of b_{bp} can be taken into account.

(5) Boundary conditions included the Sun zenith angle (computed as a function of the day, time, and latitude), the sky radiance conditions (clear-sky model [49] with an aerosol optical thickness set to a fixed value of 0.2 at 550 nm), and the sea state (wind speed of 5 m s^{-1}).

D. Selected BOUSSOLE Datasets

Four situations with increasing total chlorophyll *a* concentrations (0.13, 0.26, 0.84, and 2.23 mg m^{-3}) have been selected to show how b_{bp}, R, R_{rs}, and K_d evolve along the course of a day.

The two cases with the lowest concentrations are from summer (July–August), and the other two from the spring phytoplankton bloom (April). This selection follows the expectation that the magnitude of b_{bp} will increase, and the shape of its diel variability will change when waters become greener [18]. The four cases are for clear skies.

A larger dataset ($N = 1290$) has also been used to perform the closure experiment and then to quantify the performance of the inversions. This larger dataset includes clear-sky data collected from 9 am to 5 pm local time at all seasons and for years 2006 to 2015. The selection criteria essentially include stable physical conditions, as in [9]. Table 1 provides environmental information for this dataset.

E. Statistical Indicators

In order to assess the performances of the inversion algorithms, the following metrics were calculated, in log10 space, between retrieved and measured optical properties: the square of the Pearson correlation coefficient (r^2), the root mean square error [RMSE, Eq. (18)], the bias [i.e., the mean error, Eq. (19)], and the mean absolute error [MAE, Eq. (20)]:

Table 1. Seasonal Repartition of the Selected Dataset

	Winter (DJF)	Spring (MAM)	Summer (JJA)	Fall (SON)	Total
Number of days	9	20	28	15	72
Number of *in situ* data points	155	361	504	270	1290
[Chl] range (mg m^{-3})	0.1–1.6	0.1–3	0.1–0.6	0.1–0.8	0.1–3

$$\mathrm{RMSE} = 10^{\wedge}\left(\sqrt{\frac{\sum_{i=1}^{N}[\log_{10}(M_i)-\log_{10}(O_i)]^2}{N}}\right), \quad (18)$$

$$\mathrm{bias} = 10^{\wedge}\left(\frac{\sum_{i=1}^{N}(\log_{10}(M_i)-\log_{10}(O_i))}{N}\right), \quad (19)$$

$$\mathrm{MAE} = 10^{\wedge}\left(\frac{\sum_{i=1}^{N}|(\log_{10}(M_i)-\log_{10}(O_i))|}{N}\right), \quad (20)$$

where N is the number of measurements, M is the retrieved value, and O the measured *in situ* value, respectively.

3. RESULTS

A. Examples of Diel Variations of b_{bp}, R, R_{rs}, and K_d

The concurrent diel changes of the measured b_{bp}, R, R_{rs}, and K_d for the four selected cases are shown in Fig. 1 for $\lambda = 443$ nm and 555 nm. The b_{bp} diel cycles [Figs. 1(A)–1(D)] are characterized by a general increase as the day progresses, with minimal b_{bp} around sunrise and maximum observed 3–6 h before sunset. The relative daily changes with respect to the value at sunrise observed in b_{bp} ($\tilde{\Delta} b_{bp}$) vary between 15% and 60%. These observations are consistent with [18].

Diel variability is also observed for R and K_d at 555 nm and 443 nm whatever the trophic situation [Figs. 1(E)–1(T)], with a decrease from a maximum at sunrise to a minimum at solar noon and an increase toward another maximum at sunset. These diel variations are actually largely driven by changes in solar elevation.

Little diel variations are observed for $K_{d,n}$, which can be considered a proxy of absorption. This observation supports the hypothesis we made about a constant non-water absorption coefficient in the radiative transfer calculations. Other studies (e.g., Schallenberg *et al.* [50]) have also shown an absence of diel variations in [Chl] in other environments.

The diel variability in R_{rs}, R, and K_d measurements was calculated as the relative amplitude for each parameter from sunrise to their observed maximum during the day (Fig. 2). Overall, the ΔR values range between 15% to 55%, with a changing slope around noon whatever the wavelength [Figs. 2(A)–2(H)]. In general, the relative changes tend to increase with increasing [Chl]. The ΔK_d are generally below 15% [Figs. 2(I)–2(P)]. The $\Delta K_{d,n}$ are much smaller and do not display a significant diel cycle.

B. Optical Closure

As mentioned previously, optical closure was performed on a larger dataset in order to verify the consistency of the measured AOPs and b_{bp}. The comparison indicates good agreement (Fig. 3, Table 2) confirming consistency of the dataset.

Furthermore, the diel changes of the modeled R and K_d compare well with those of the field determinations (red *versus* black curves in Fig. 1), except perhaps when the assumption of no diel changes in [Chl] is invalid, i.e., for the highest [Chl] values [Figs. 2(H), 2(L), 2(P), and 2(T)]. This consistency among field measurements of b_{bp} and AOPs indicates that it can be

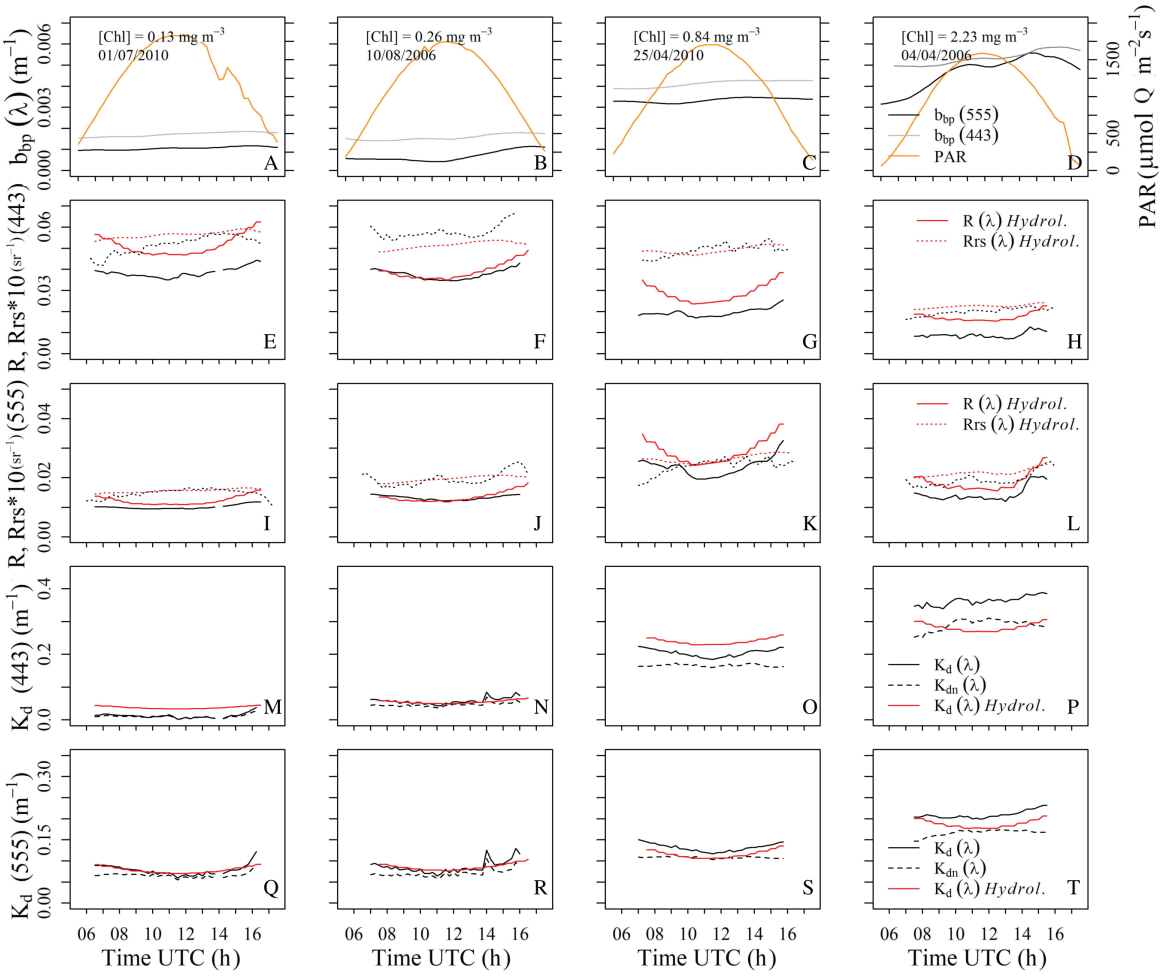

Fig. 1. Examples of daily changes of b_{bp} (A)–(D), sampling dates and daily course of PAR, orange line, are displayed too), R and R_{rs} (E)–(L), and K_d (M)–(T) at 443 and 555 nm. The continuous black curves are for the measured quantities (except R_{rs}, dotted curve), the dashed black curves for the normalized values ($K_{d,n}$), and the red curves for the R and K_d values obtained from radiative transfer computations.

reasonably expected that an accurate numerical inversion of the measured AOPs would be capable of retrieving the diel changes observed for b_{bp}.

C. Retrieving b_{bp} and Its Diel Cycle

The results obtained with the three algorithms are first displayed for the full dataset, irrespective of how the diel variability is retrieved (Fig. 4).

Overall, good results for the QAA and GSM algorithms are obtained in the blue ($\lambda = 443$ nm) and the green ($\lambda = 555$ nm) [Figs. 4(C), 4(D), 4(E), and 4(F)], whereas the MOR algorithm showed only a good comparison at 555 nm [Figs. 4(A) and 4(B)], (Table 2).

Nevertheless, degraded performances appear for the QAA and GSM algorithms in the low range for $\lambda = 555$ nm, with a significant overestimation of b_{bp} values < 0.001 m^{-1} [Figs. 4(D) and 4(F)], whereas MOR still works reasonably well [Fig. 4(B)]; significant dispersion but lower bias).

These results also show that it is difficult to get accurate estimations of b_{bp} in the blue by using only blue bands for the inversion [MOR, Fig. 4(A)], whereas better results are obtained when using methods that constrain the b_{bp} derivation using more spectral bands [QAA and GSM; Figs. 4(C) and 4(E)].

The comparison between the b_{bp} values obtained from inversion of the measured R and K_d or R_{rs} and their measured values for the four case studies is shown in Figs. 5(A)–5(D) for $\lambda = 443$ nm and Figs. 5(E)–5(H) for $\lambda = 555$ nm. Again, the best results are obtained at 555 nm. Although the retrieved values generally reproduce the observed daytime increase of b_{bp}, significant differences are observed in the amplitude of b_{bp} [e.g., Fig. 5(G)] and in the shape of its diel changes [e.g., Fig. 5(A)].

The results for the same four examples are also displayed in relative amplitudes of the diel change in b_{bp} from sunrise, $\tilde{\Delta} b_{bp}$, as calculated either from direct measurements or from AOPs inversion [Figs. 6(A)–6(D)] for $\lambda = 443$ nm and Figs. 6(E)–6(H) for $\lambda = 555$ nm]. The retrieved values are higher by a factor of $1.4 \pm 0.5\%$ in the green and of $1.7 \pm 1.1\%$ in the blue with respect to measured values.

Finally, the comparison between the relative amplitude calculated from modeled and from measured b_{bp} data has been extended beyond the four case studies here selected, by applying the inversion to a larger dataset (see Section 2.D and Table 1).

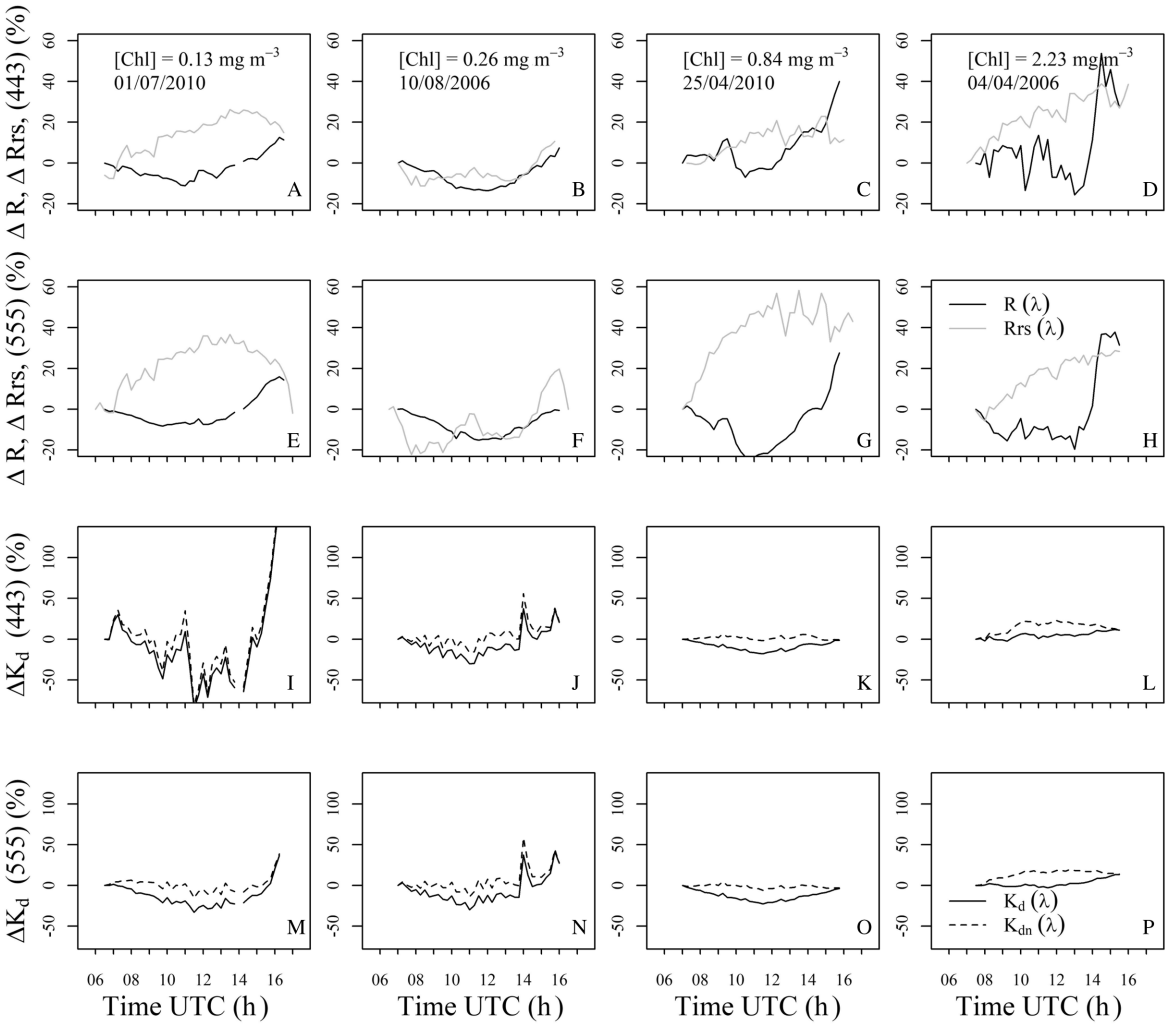

Fig. 2. Examples of daily relative changes (%) of ΔR (black line; (A)–(D) at 443 nm, (E)–(H) at 555 nm), ΔR_{rs} (gray line; (A)–(D) at 443 nm, (E)–(H) at 555 nm), and ΔK_d at 443 nm (I)–(L) and ΔK_d at 555 nm (M–P). The dashed black curves in panels I–P are for the normalized values ($K_{d,n}$).

The comparison shows that it is possible to obtain satisfactory values of $\tilde{\Delta} b_{bp}$ at 555 nm (Fig. 7(B), whereas the performances at 443 nm are poorer [Fig. 7(A)], although this is largely due to the lower performance of MOR at 443 nm (Table 3). We also looked at the comparison between the absolute diel changes of b_{bp}, [Δb_{bp}], calculated either from modeled or measured data at 443 and 555 nm [Figs. 7(C) and 7(D)]. Unsurprisingly, we observed a better accuracy in the green [Fig. 7(D)] than in the blue [Fig. 7(C)] (Table 3).

4. DISCUSSION AND CONCLUSIONS

Our case study has shown that the amplitude of the b_{bp} diel cycle observed *in situ* is large enough to generate a measurable diel variability in reflectance. Although this result could be anticipated because the reflectance is at first order proportional to b_b, it still had to be verified quantitatively. Reflectance is, however, also inversely proportional to absorption. Diel increases in absorption would have to parallel those in b_{bp} to make their ratio, and then the reflectance, little variable over the day. This is not what we observe, suggesting that possible changes in absorption are not large enough to counterbalance those in b_{bp} in shaping the diel variability of reflectance. If absorption would evolve in the opposite way to b_{bp}, which is not *a priori* expected, the result would be to enhance the diel variability in reflectance. The closure calculations have confirmed that the diel changes in AOPs could be well reproduced by accounting only for diel changes in b_{bp}, ignoring possible diel changes in absorption.

However, significant differences were observed between the b_{bp} values retrieved from AOPs and those obtained from the *in situ* measurements, questioning whether the performance of the inversion algorithms are good enough to allow deriving rather small daily changes of b_{bp} from AOPs measurements taken at different times of a day. These inaccuracies are not specific to the four case studies selected here, as if their selection would have been inappropriate. When the inversion algorithms were applied to a larger dataset, the retrieved *versus* measured b_{bp} values show a significant dispersion (Fig. 4, Table 2). In particular, MOR performs better in the green (i.e., 555 nm) [$r^2 = 0.67$, Fig. 4(B)] with no noticeable degradation for low b_{bp} values,

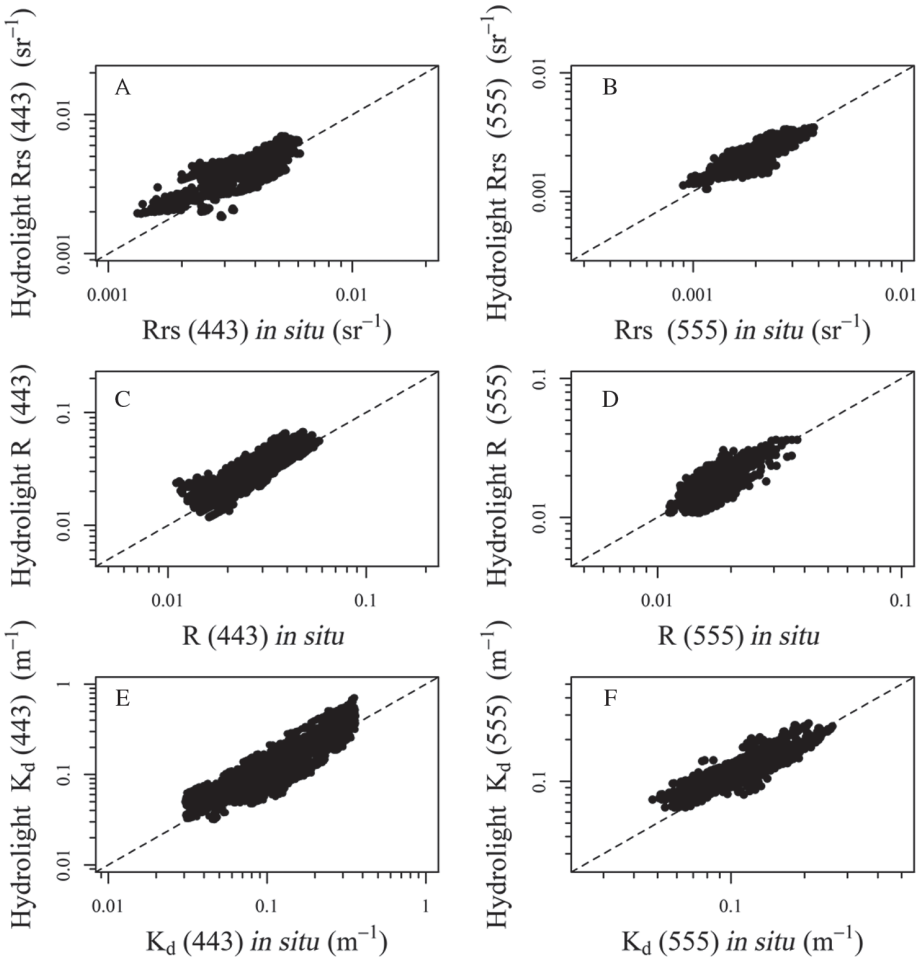

Fig. 3. R_{rs} (top row), R (middle), and K_d (bottom) values computed by HydroLight compared to those measured *in situ* at 443 nm (A), (C, (E) and at 555 nm (B), (D, (F).

Table 2. Statistics for the Comparisons Presented in Figs. 3 and 4: Number of Points (N), Correlation Coefficient (r^2), bias, Mean Absolute Error (MAE), and Root Mean Square Error (RMSE)

λ	N	r^2	bias	MAE	RMSE
HydroLight R_{rs} versus in situ R_{rs}					
443	1290	0.78	1.16	1.22	1.27
555	1290	0.79	1.04	1.10	1.13
HydroLight R versus in situ R					
443	1290	0.72	1.12	1.19	1.24
555	1290	0.79	0.97	1.13	1.16
HydroLight K_d versus in situ K_d					
443	1290	0.71	1.19	01.20	1.26
555	1290	0.81	1.09	1.16	1.20
b_{bp} retrieved versus in situ b_{bp}					
MOR					
443	1290	0.37	1.35	1.45	1.53
555	1290	0.67	0.86	1.25	1.33
QAA					
443	967	0.67	1.33	1.34	1.41
555	967	0.65	1.40	1.60	1.72
GSM					
443	1003	0.49	0.88	1.34	1.32
555	1003	0.48	1.36	1.41	1.53

as compared to the blue [$r^2 = 0.37$ instead of 0.67; Fig. 4(A)]. These results are questioning the possibility to obtain accurate estimations of b_{bp} at 443 nm using Eq. (16) in oligotrophic waters.

It could be, however, hypothesized that these inaccuracies would not change when inverting AOPs taken at different times of a day, so that they only marginally affect the retrieval of the quantity of interest here, namely the daily change in b_{bp} and ultimately the daily change in POC, ΔPOC.

This hypothesis seems confirmed in the green for MOR, where $\tilde{\Delta} b_{bp}$ and ΔPOC are retrieved with good accuracy [Figs. 7(B) and 8(B)] but, again, not in the blue, where a large dispersion is observed [Figs. 7(A) and 8(A)]. Therefore, using only the blue part of the spectrum is likely inappropriate to perform inversion of R and K_d in view of deriving $\tilde{\Delta} b_{bp}$. The QAA and GSM algorithms provide similarly good results in the green [Figs. 7(B) and 8(D), 8(F), Table 3] and better estimates in the blue region [Figs. 7(A), 7(C) and Figs. 8(C), 8(E), and Table 3] as compared to MOR.

As far as the $R - K_d$ algorithm (i.e., MOR) is concerned, the conclusions can be tempered, however, by reminding that the algorithm was not operated in ideal conditions, i.e., a single [Chl] value has been used for a given day to derive μ_d and f' from lookup tables, whereas the actual [Chl] value at a given

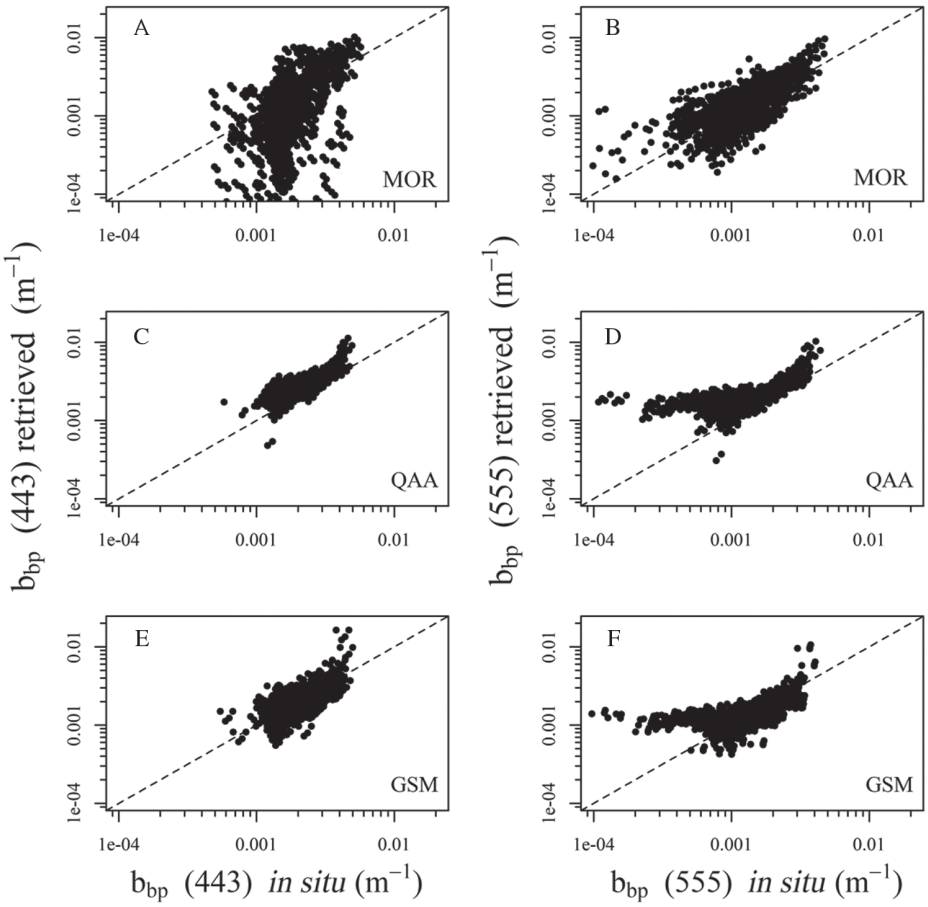

Fig. 4. b_{bp} retrieved from inversion of AOPs as a function of the measured b_{bp}, for $\lambda = 443$ nm (A), (C, (E) and $\lambda = 555$ nm (B), (D), (F). Results are shown for the three inversion algorithms, as indicated on each panel. The dashed line is the 1:1 line.

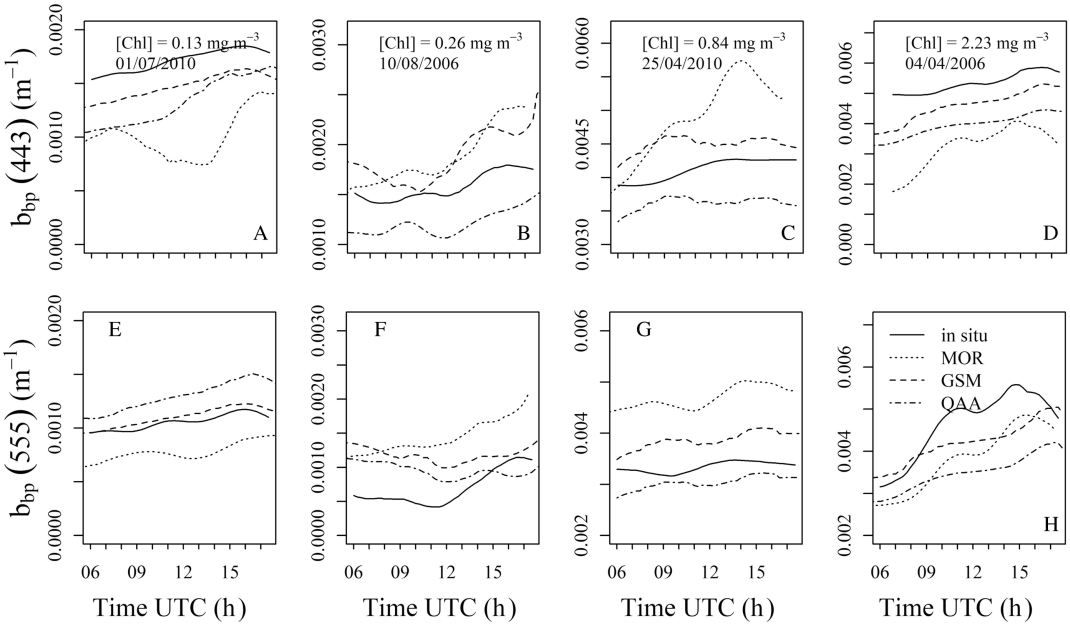

Fig. 5. Daily changes in measured b_{bp} (solid curves) and in the values retrieved with the three inversion algorithms (as indicated on panel H), for the four case studies.

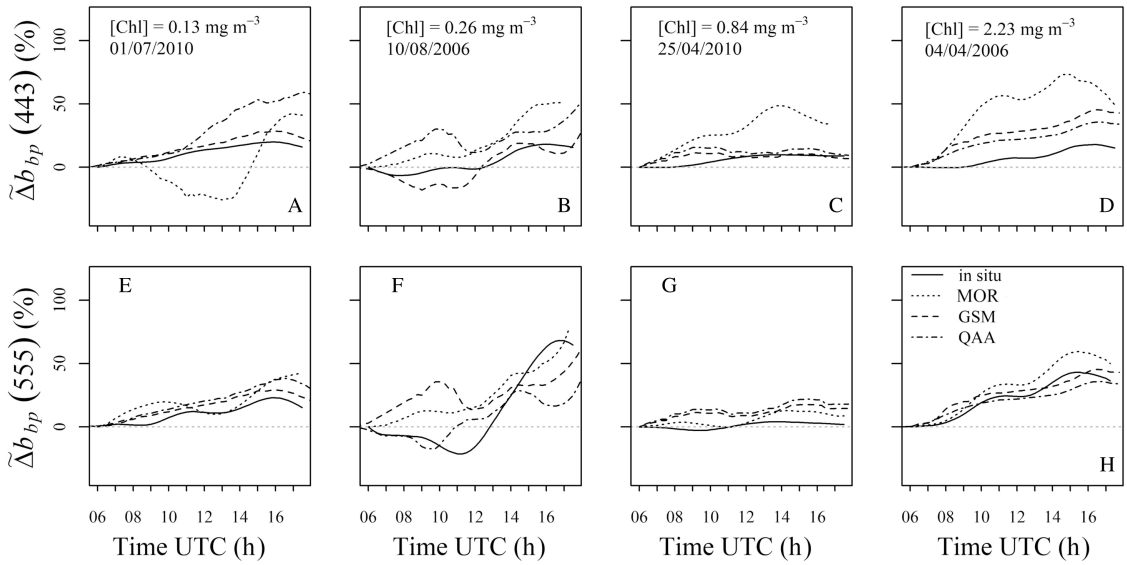

Fig. 6. As in Fig. 5 but for the relative change in b_{bp} from sunrise.

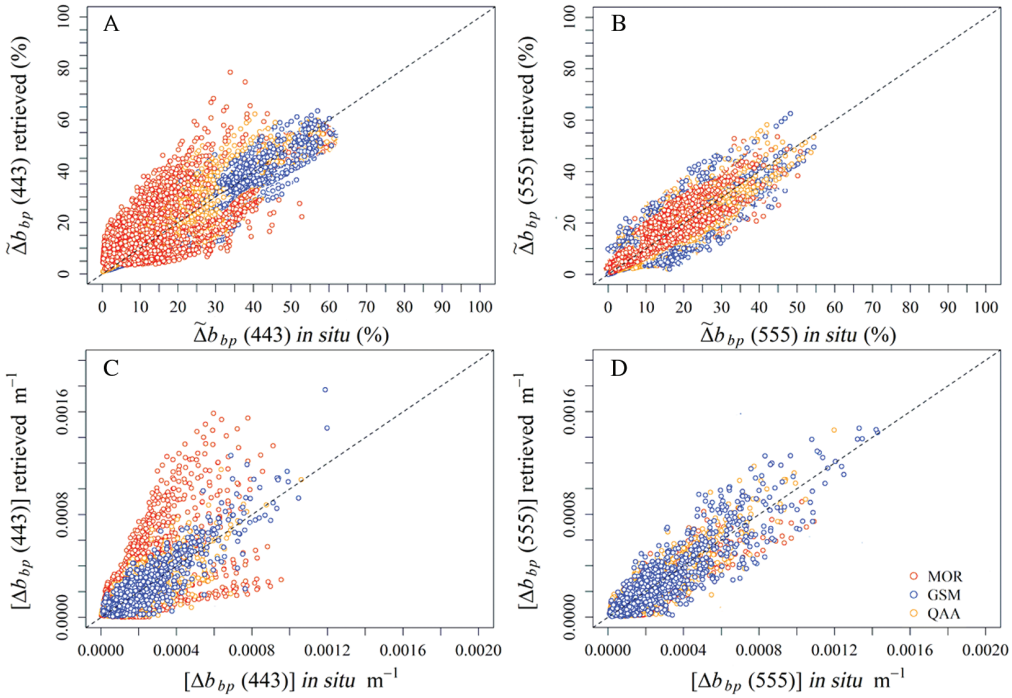

Fig. 7. (A), (B), $\tilde{\Delta}b_{bp}$ calculated from b_{bp} values obtained from inversion of AOPs using the three algorithms, as a function of the same quantity derived from the field measurements. (A) is for $\lambda = 443$ nm, (B) is for $\lambda = 555$ nm, and the color coding is indicated in panel (D). (C), (D), as in (A), (B) but for the absolute diel change of b_{bp}. The dashed line is the 1:1 line.

time of the day should in principle have been used to perform the $R - K_d$ inversion at that time. High-frequency measurements of [Chl] are, however, rarely carried out at sea, and diurnal variations of [Chl] are poorly documented. The chlorophyll fluorescence signal neither can be used to assess these changes in surface waters because it is impacted by non-photochemical quenching. Corrections can be applied, e.g., [51], but their performance is difficult to assess. It cannot be excluded that such variability exists, however, and that ignoring it could lead to uncertainties in the retrieved b_{bp} values [52,53].

Would the MOR algorithm be ideally applied, i.e., being fed with high-accuracy measurements of R, K_d, and [Chl] in view of deriving b_{bp} at several times of a day, the b_{bp} diel cycle might still be incorrectly retrieved. Average bio-optical relationships are built-in in such a [Chl]-based algorithm ([30] in the present case), which makes it incapable of accounting for local variations in the bio-optical relationships for a given water body at a given time of the day. The non-water total absorption per unit of [Chl] has reasonable chances to change as the photosynthetic process evolves during the day, for instance. Similarly, the backscattering

Table 3. Number of Points (*N*), Correlation Coefficient (r^2), bias, Mean Absolute Error (MAE), and Root Mean Square Error (RMSE), Values Corresponding to Data Displayed in Figs. 7 and 8

λ	*N*	r^2	bias	MAE	RMSE
$[\Delta b_{bp}]$ *retrieved versus in situ* $[\Delta b_{bp}]$					
MOR					
443	1290	0.37	1.12	2.28	2.83
555	1290	0.78	0.86	1.61	1.78
QAA					
443	967	0.71	1.08	1.53	1.75
555	967	0.76	1.17	1.44	1.64
GSM					
443	1003	0.73	1.17	1.44	1.65
555	1003	0.79	0.91	1.49	1.75
ΔPOC *retrieved versus in situ* ΔPOC					
MOR					
443	1290	0.37	1.13	1.85	2.07
555	1290	0.78	1.03	1.39	1.43
QAA					
443	967	0.71	1.07	1.38	1.46
555	967	0.76	0.92	1.22	1.31
GSM					
443	1003	0.71	1.19	1.42	1.51
555	1003	0.77	0.87	1.36	1.47

ratio likely changes when phytoplankton grows and detritus are generated. As a consequence, the μ_d and f' values extracted from lookup tables based on [Chl] might become inappropriate if the [Chl]-to-IOPs relationships embedded in the model differ significantly from the actual ones. These errors are among the likely causes of the dispersion observed in Fig. 7, for instance.

Such errors are usually considered as the unavoidable uncertainties in bio-optical inversions, however acceptable when inversion algorithms are only evaluated in their ability to derive inherent optical properties over several orders of magnitude changes. More subtle changes in IOPs (b_{bp}) are here sought after, so that errors considered as acceptable when aiming at a global picture may become excessive when aiming at quantifying diel variability. This issue is not specific to the inversion algorithms used in this study, but rather inherent to most inversion algorithms currently used, which all include, at various degrees, some empirical parameterizations. The inversion of radiometric measurements in view of deriving the diel b_{bp} variability is therefore seriously challenged. Whatever their rationale and implementation, inversion algorithms would have to rely as little as possible on bio-optical relationships established from global databases if they were to be used to derive diel variability of b_{bp}. For instance, an algorithm such as the one used here [Eqs. (16) and (17)] could be modified so that lookup tables for μ_d and f' are indexed on IOPs instead of [Chl], following

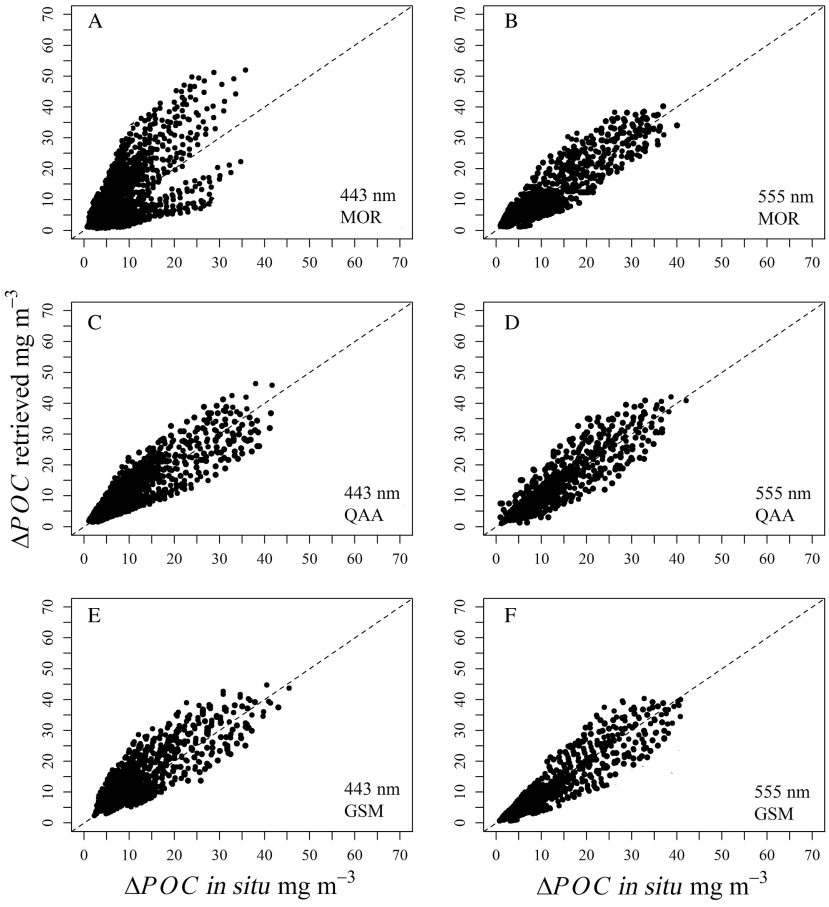

Fig. 8. Diel change of POC calculated from the diel change in b_{bp}, where b_{bp} was retrieved from inversion of AOPs, as a function of the same quantity derived from the field measurements. (A), (C), and (E) are for λ = 443 nm and the MOR, QAA, and GSM algorithms, respectively. (B), (D), and (F) are for λ = 555 nm and the same three algorithms. The dashed line indicates the 1:1 line.

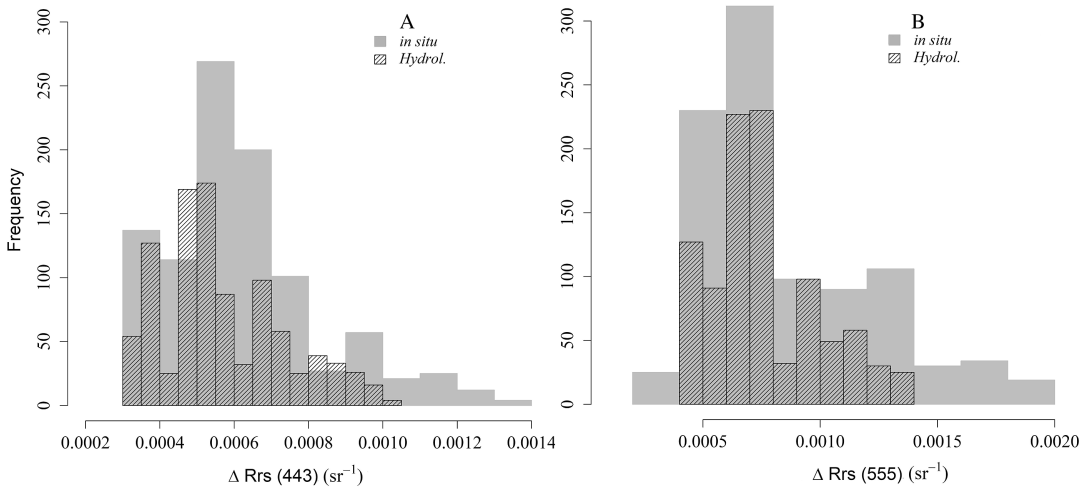

Fig. 9. R_{rs} changes from its morning value to when it reaches its daily maximum, for $\lambda = 443$ nm (A) and $\lambda = 555$ nm (B). The hatched histogram is for the simulated data and the grayed histogram for the measurements.

a similar logic as the one proposed by the IOP-based approach of Lee *et al.* [54]. Another example going in that direction is the ZTT model [55].

The results presented here are based on high-quality field measurements. In the satellite configuration, however, the ocean reflectance is obtained after the top-of-atmosphere satellite observations have been corrected from atmosphere effects. It was here implicitly assumed that this atmospheric correction can be accurately carried out, so that the reflectance spectrum is obtained within the desired uncertainty at any time of the day. The impact of violation of this significant assumption is out of scope here and would require a dedicated study. We did a preliminary assessment of this question, however, by comparing the diel R_{rs} changes in our dataset and associated radiative transfer simulations (Fig. 9) to typical uncertainties in atmospheric corrections at the BOUSSOLE site, as reported in [20]. The root mean square errors in their Tables 2–4 are of about 0.001 to 0.0017 sr^{-1} at 443 nm and $0.0004 - 0.0005$ sr^{-1} at 555 nm [values in that paper are reported as $\rho = \pi\ R_{rs}$; their Eq. (6)]. These values are above the ΔR_{rs} shown in Fig. 9 for $\lambda = 443$ nm, suggesting that blue bands are not good candidates for retrieval of the R_{rs} diel variability. On the contrary, the R_{rs} uncertainty at 555 nm is below the ΔR_{rs} shown in Fig. 9 for that wavelength. Random uncertainties are not necessarily the best measure to use here, however. Indeed, for given atmospheric conditions, inaccuracies of the atmospheric correction generally lead to consistent, either positive or negative, biases over the visible range, generally increasing toward shorter wavelengths. In such a case, the magnitude of the atmospheric correction error will matter less than its change as the solar elevation evolves over the day, resulting or not in masking the diel changes.

It should also be kept in mind that the BOUSSOLE dataset includes a majority of oligotrophic conditions, so that inversion algorithms were applied in conditions of low IOP values and a small diurnal signal. We should not, therefore, rule out the possibility to more accurately retrieve diel b_{bp} cycles from inversion of measured AOPs on the basis of this sole dataset. Major upwelling areas, as well as basin-scale phytoplankton blooms, e.g., the northern Atlantic spring bloom, are areas where the b_{bp} values and the amplitude of their diel cycle are higher, so that b_{bp} could be retrieved with better accuracy than what is shown here. Specific studies of the diel variability of IOPs and daily changes in AOPs are therefore needed in such areas. Whenever feasible, they should include measurements of the quantities that are necessary to apply the algorithm with the desired inputs, such as measurements at high frequency of absorption or [Chl].

Funding. Agence Nationale de la Recherche; European Space Agency; Centre National d'Etudes Spatiales; Centre National de la Recherche Scientifique; Institut national des sciences de l'Univers; Sorbonne Université, Institut de la Mer de Villefranche (IMEV); Conseil Régional Provence-Alpes-Côte d'Azur.

Acknowledgment. The authors are grateful to the BOUSSOLE technical staff for their work in performing buoy deployments and maintenance, monthly cruises, and laboratory analyses. Our thanks go in particular to Emilie Diamond and Melek Golbol for the monthly cruises, and to Joséphine Ras, Céline Dimier, and Mustapha Ouhssain for the phytoplankton pigment analyses (SAPIGH analytical platform of the Laboratoire d'Océanographie de Villefranche, CNRS, France). This study is a contribution to the ANR Bio-optics and Carbon Experiment (BIOCAREX) and BOUSSOLE projects. Finally, we are grateful to the external reviewers for providing constructive comments to the paper.

Disclosures. The authors declare no conflicts of interest.

Data availability. Data presented in the paper can be obtained from the BOUSSOLE dataset, available in Ref. [22]. Other generated modeled data may be obtained upon request.

REFERENCES

1. J.-K. Choi, Y. J. Park, J. H. Ahn, H.-S. Lim, J. Eom, and J.-H. Ryu, "GOCI, the world's first geostationary ocean color observation satellite, for the monitoring of temporal variability in coastal water turbidity," J. Geophys. Res. **117**, 2156–2202 (2012).
2. Y. Y. H. Ahn, J. H. Ryu, S. I. Cho, and S. H. Kim, "Missions and user requirements of the 2nd Geostationary Ocean Color Imager (GOCI-II)," Korean J. Remote Sens. **26**, 277–285 (2010).
3. J. H. Ahn and Y.-J. Park, "Estimating water reflectance at near-infrared wavelengths for turbid water atmospheric correction: a preliminary study for GOCI-II," Remote Sens. **12**, 3791 (2020).

4. National Aeronautics and Space Administration, "NASA targets coastal ecosystems with new space sensor," 2019, https://www.nasa.gov/press-release/nasa-targets-coastal-ecosystems-with-new-space-sensor.
5. D. Antoine, "Ocean-colour observations from a geostationary orbit," in Reports and Monographs of the International Ocean-Colour Coordinating Group, , IOCCG Report No. 12 (IOCCG, 2012).
6. K. Ruddick, G. Neukermans, Q. Vanhellemont, and D. Jolivet, "Challenges and opportunities for geostationary ocean colour remote sensing of regional seas: a review of recent results," Remote Sens. Environ. **146**, 63–76 (2014).
7. D. A. Siegel, T. D. Dickey, L. Washburn, M. K. Hamilton, and B. G. Mitchell, "Optical determination of particulate abundance and production variations in the oligotrophic ocean," Deep-Sea Res. **36**, 211–222 (1989).
8. H. Claustre, A. Morel, M. Babin, C. Cailliau, D. Marie, J.-C. Marty, and D. Vaulot, "Variability in particle attenuation and stimulated fluorescence in the tropical and equatorial Pacific: scales, patterns and some biogeochemical implications," J. Geophys. Res. **104**, 3401–3422 (1999).
9. P. Gernez, D. Antoine, and Y. Huot, "Diel cycles of the particulate beam attenuation coefficient under varying trophic conditions in the northwestern Mediterranean Sea: observations and modeling," Limnol. Oceanogr. **56**, 17–36 (2011).
10. H. Loisel, V. Vantrepotte, K. Norkvist, X. Mériaux, M. Kheireddine, J. Ras, M. Pujo-Pay, Y. Combet, K. Leblanc, G. Dall'Olmo, R. Mauriac, D. Dessailly, and T. Moutin, "Characterization of the bio-optical anomaly and diurnal variability of particulate matter, as seen from scattering and backscattering coefficients, in ultra-oligotrophic eddies of the Mediterranean Sea," Biogeosciences **8**, 3295–3317 (2011).
11. H. Loisel and A. Morel, "Light scattering and chlorophyll concentration in case 1 waters: a re-examination," Limnol. Oceanogr. **43**, 847–857 (1998).
12. M. Barnes and D. Antoine, "Proxies of community production derived from the diel variability of particulate attenuation and backscattering coefficients in the northwest Mediterranean Sea," Limnol. Oceanogr. **59**, 2133–2149 (2014).
13. D. Stramski and R. A. Reynolds, "Diel variations in the optical properties of a marine diatom," Limnol. Oceanogr. **38**, 1347–1364 (1993).
14. M. D. Durand and R. J. Olson, "Diel patterns in optical properties of the chlorophyte Nannochloris sp.: relating individual-cell to bulk measurements," Limnol. Oceanogr. **43**, 1107–1118 (1998).
15. M. D. Durand, R. E. Green, H. M. Sosik, and R. J. Olson, "Diel variations in optical properties of Micromonas pusilla (Prasinophyceae)," J. Phycol. **38**, 1132–1142 (2002).
16. M. J. Behrenfeld and E. Boss, "Beam attenuation and chlorophyll concentration as alternative optical indices of phytoplankton biomass," J. Mar. Res. **64**, 431–451 (2006).
17. A. Morel and L. Prieur, "Analysis of variations in ocean color," Limnol. Oceanogr. **22**, 709–722 (1977).
18. M. Kheireddine and D. Antoine, "Diel variability of the particulate beam attenuation and backscattering coefficients in the northwestern Mediterranean Sea (BOUSSOLE site)," J. Geophys. Res. **119**, 5465–5482 (2014).
19. D. Antoine, M. Chami, H. Claustre, F. D'Ortenzio, A. Morel, G. Becu, B. Gentili, F. Louis, J. Ras, E. Roussier, A. J. Scott, D. Tailliez, S. B. Hooker, P. Guevel, J. F. Deste, C. Dempsey, and D. Adams, "BOUSSOLE: a joint CNRS-INSU, ESA, CNES and NASA ocean color calibration and validation activity," in *NASA Technical memorandum* (2006), p. 61.
20. D. Antoine, F. D'Ortenzio, S. B. Hooker, G. Becu, B. Gentili, D. Tailliez, and A. J. Scott, "Assessment of uncertainty in the ocean reflectance determined by three satellite ocean color sensors (MERIS, SeaWiFS and MODIS-A) at an offshore site in the Mediterranean Sea (BOUSSOLE project)," J. Geophys. Res. **113**, 2156–2202 (2008).
21. D. Antoine, P. Guevel, J. F. Deste, G. Becu, F. Louis, A. J. Scott, and P. Bardey, "The 'BOUSSOLE' buoy–a new transparent-to-swell taut mooring dedicated to marine optics: Design, tests, and performance at sea," J. Atmos. Ocean. Tech. **25**, 968–989 (2008).
22. M. Golbol, V. Vellucci, and D. Antoine, "BOUSSOLE data set," French Oceanographic Cruises, (2020), https://doi.org/10.18142/1.
23. R. A. Maffione and D. R. Dana, "Instruments and methods for measuring the backward-scattering coefficient of ocean waters," Appl. Opt. **36**, 6057–6067 (1997).
24. A. Morel, B. Gentili, M. Chami, and J. Ras, "Bio-optical properties of high chlorophyll case 1 waters and of yellow-substance-dominated case 2 waters," Deep Sea Res. **53**, 1439–1459 (2006).
25. E. Boss and W. S. Pegau, "Relationship of light scattering at an angle in the backward direction to the backscattering coefficient," Appl. Opt. **40**, 5503–5507 (2001).
26. D. R. Dana and R. A. Maffione, "Determining the backward scattering coefficient with fixed-angle backscattering sensors? Revisited," in *Ocean Optics XVI Conference*, Santa Fe, New Mexico, USA, 18–22 November, 2002.
27. X. D. Zhang and L. B. Hu, "Estimating scattering of pure water from density fluctuation of the refractive index," Opt. Express **17**, 1671–1678 (2009).
28. X. D. Zhang, L. B. Hu, and M. X. He, "Scattering by pure seawater: effect of salinity," Opt. Express **17**, 5698–5710 (2009).
29. A. Bricaud, A. Morel, and L. Prieur, "Absorption by dissolved organic matter of the sea (yellow substance) in the UV and visible domains," Limnol. Oceanogr. **26**, 43–53 (1981).
30. A. Morel and S. Maritorena, "Bio-optical properties of oceanic waters: a reappraisal," J. Geophys. Res. **106**, 7163–7180 (2001).
31. J. Ras, H. Claustre, and J. Uitz, "Spatial variability of phytoplankton pigment distributions in the Subtropical South Pacific Ocean: comparison between in situ and predicted data," Biogeosciences **5**, 353–369 (2008).
32. R. W. Austin, "The remote sensing of spectral radiance from below the ocean surface," in *Optical Aspects of Oceanography*, N. G. Jerlov and E. Steemann Nielsen, eds. (Academic, 1974), pp. 317–344.
33. E. Leymarie, C. Penkerc'h, V. Vellucci, C. Lerebourg, D. Antoine, E. Boss, M. R. Lewis, F. D'Ortenzio, and H. Claustre, "ProVal: a new autonomous profiling float for high quality radiometric measurements," Front. Mar. Sci. **5**, 437 (2018).
34. A. Białek, V. Vellucci, B. Gentil, D. Antoine, J. Gorroño, N. Fox, and C. Underwood, "Monte Carlo–based quantification of uncertainties in determining ocean remote sensing reflectance from underwater fixed-depth radiometry measurements," J. Atmos. Ocean. Technol. **37**, 177–196 (2020).
35. C. D. Mobley, *Light and Water: Radiative Transfer in Natural Waters* (Elsevier, 1994).
36. A. Morel, D. Antoine, and B. Gentili, "Bidirectional reflectance of oceanic waters: accounting for Raman emission and varying particle scattering phase function," Appl. Opt. **41**, 6289–6306 (2002).
37. H. R. Gordon, O. B. Brown, and M. M. Jacobs, "Computed relationships between inherent and apparent optical-properties of a flat homogeneous ocean," Appl. Opt. **14**, 417–427 (1975).
38. H. R. Gordon, "Can the Lambert-Beer law be applied to the diffuse attenuation coefficient of ocean water," Limnol. Oceanogr. **34**, 1389–1409 (1989).
39. A. Morel and B. Gentili, "Radiation transport within oceanic (case 1) water," J. Geophys. Res. **109**, C06008 (2004).
40. A. Morel and B. Gentili, "Diffuse reflectance of oceanic waters–its dependence on sun angle as influenced by the molecular scattering contribution," Appl. Opt. **30**, 4427–4438 (1991).
41. Z. Lee, K. L. Carder, and R. A. Arnone, "Deriving inherent optical properties from water color: a multiband quasi-analytical algorithm for optically deep waters," Appl. Opt. **41**, 5755–5772 (2002).
42. H. R. Gordon and A. Morel, *Remote Assessment of Ocean Color for Interpretation of Satellite Visible Imagery: A Review*, Lecture notes on coastal and estuarine studies (Springer, 1983).
43. S. A. Garver and D. A. Siegel, "Inherent optical property inversion of ocean color spectra and its biogeochemical interpretation: 1. Time series from the Sargasso Sea," J. Geophys. Res. **102**, 18607–18625 (1997).
44. S. Maritorena, D. A. Siegel, and A. R. Peterson, "Optimal tuning of a semi-analytical model for global applications," Appl. Opt. **41**, 2705–2714 (2002).
45. International Ocean-Color Coordinating Group (IOCCG), "Remote sensing of inherent optical properties: fundamentals, tests of algorithms, and applications," in *Reports of the International Ocean-Colour Coordinating Group IOCCG No5*, Z. Lee, ed. (2006).

46. P. Lee, C. Hu, S. Shang, K. Du, M. Lewis, R. Arnone, and R. Brewin, "Penetration of UV-visible solar radiation in the global oceans: insights from ocean color remote sensing," J. Geophys. Res. Oceans **118**, 4241–4255 (2013).
47. R. M. Pope and E. S. Fry, "Absorption spectrum (380-700 nm) of pure water. 2. Integrating cavity measurements," Appl. Opt. **36**, 8710–8723 (1997).
48. A. Morel, "Optical properties of pure water and pure sea water," in *Optical Aspects of Oceanography*, N. G. Jerlov and E. S. Nielsen, eds. (Academic, 1974), pp. 1–23.
49. W. W. Gregg and K. L. Carder, "A simple spectral solar irradiance model for cloudless maritime atmospheres," Limnol. Oceanogr. **35**, 1657–1675 (1990).
50. C. Schallenberg, R. F. Strzepek, N. Schuback, L. A. Clementson, P. W. Boyd, and T. W. Trull, "Diel quenching of Southern ocean phytoplankton fluorescence is related to iron limitation," Biogeosciences **17**, 793–812 (2020).
51. L. Carberry, C. Roesler, and S. Drapeau, "Correcting in situ chlorophyll fluorescence time-series observations for nonphotochemical quenching and tidal variability reveals nonconservative phytoplankton variability in coastal waters," Limnol. Oceanogr. Methods **17**, 462–473 (2019).
52. M. Ragni and M. R. d'Alcalà, "Circadian variability in the photobiology of Phaeodactylum tricornutum: pigment content," J. Plank. Res. **29**, 141–156 (2007).
53. C. Poulin, Z. Xiaodong, Y. Ping, and Y. Huot, "Diel variations of the attenuation, backscattering and absorption coefficients of four phytoplankton species and comparison with spherical, coated spherical and hexahedral particle optical models," J. Quant. Spectrosc. Radiat. Transfer **217**, 288–304 (2018).
54. Z. P. Lee, K. Du, K. J. Voss, G. Zibordi, B. Lubac, R. Arnone, and A. Weidemann, "An inherent-optical-property-centered approach to correct the angular effects in water-leaving radiance," Appl. Opt. **50**, 3155–3167 (2011).
55. M. Twardowski and A. Tonizzo, "Ocean color analytical model explicitly dependent on the volume scattering function," Appl. Sci. **8**, 2684 (2018).